Biosensors and Bioelectronics 92 (2017) 171–178

Contents lists available at ScienceDirect

Biosensors and Bioelectronics

journal homepage: www.elsevier.com/locate/bios

TiO_2 nanowire arrays modified with a simultaneous "etching, doping and deposition" technique for ultrasensitive amperometric immunosensing

Xiaoqiang Liu[a,*], Xiaohe Huo[a], Peipei Liu[a], Yunfei Tang[a], Jun Xu[a], Huangxian Ju[b,*]

[a] Institute of Environmental and Analytical Sciences, College of Chemistry and Chemical Engineering, Henan University, Kaifeng, Henan Province 475004, PR China

[b] State Key Laboratory of Analytical Chemistry for Life Science, Department of Chemistry, Nanjing University, Nanjing 210023, PR China

ARTICLE INFO

Keywords:
Amperometry
Immunosensor
MoS_2
TiO_2 nanowire arrays
TiO_2 nanorod
Carcinoembryonic antigen

ABSTRACT

In this work, an ultrasensitive immunosensing scaffold was structured with TiO_2 nanowire (TiNW) arrays modified with molybdenum (Mo) and MoS_2 flakes by a triplex "etching, doping and deposition" technique. The triply modification of TiNW arrays improved their electron transfer, and the decoration of MoS_2 flakes on TiNW arrays increased both the conductivity and the specific surface area of TiNW. Accordingly, the triply modified TiNW arrays provided a biocompatible microenviroment for the biomolecules and high specific surface area to load big amount of biomolecules. The immunosensor was prepared by immobilizing capture antibody on the scaffold surface with double amino-reactive crosslinker, and the tracing labels were prepared by immobilizing signal antibody and horseradish peroxidase molecules on cylinder-shaped TiO_2 nanorods. After sandwich-type immunoreaction, the tracing labels were quantitatively captured on the immunosensor surface for the detection of carcinoembryonic antigen as a model analyte. This amperometric method showed a linear range of 0.001 and 150 ng mL^{-1} with a detection limit of 0.5 pg mL^{-1}. This work provided a promising platform for sensitive amperometric immunosensing of protein biomarkers.

1. Introduction

Sensitive determination of tumor biomarkers plays an important role in screening, diagnosis and clinical management of cancers because their elevated levels in blood serum are usually associated with certain potential cancers (Darain et al., 2003; Freedland, 2011; Tang et al., 2010). For example, carcinoembryonic antigen (CEA), a highly glycosylated protein, has been used as a biomarker for lung, colorectal, liver, pancreatic and breast cancers (Rong et al., 2016). Therefore, developing a highly effective detection method for tumor biomarkers is of immense significance in clinical medicine. One of the most efficient detection methods for tumor biomarkers was reported to be the electrochemical immunoassay, which exhibited many merits including high sensitivity, low cost, simple instrumentation and good portability (Marquette and Blum, 2006; Zhang et al., 2007). In recent years, the analytical performance of the electrochemical immunosensors has been greatly improved with the continuous development of the nanoscience and nanotechnology (Li et al., 2017; Ramanathan et al., 2016; Wang et al., 2015). Among the nanomaterials applied in immunosensors, titanium dioxide (TiO_2) has become a hot research spot due to its high chemical stability, excellent biocompatibility, environmental friendliness, strong photocatalytic capability and easy preparation (Huo et al., 2016; Wang et al., 2009; Zhao et al., 2014; Zhuo et al., 2011). For instance, Gao et al. (2013) developed an electrochemical immunosensor for rabbit immunoglobulin G using TiO_2 nanotube arrays as the sensor platform and HRP labeled antibody-Au nanoparticles as the signal probe. The synergetic effect attributed to TiO_2 nanotubes and HRP-Au nanoparticles has effectively improved the immunosensor performance.

As a new type of TiO_2 nanostructures, TiO_2 nanowire (TiNW) array has widely been used to develop various photoelectrochemical sensors (Da et al., 2014; Xu et al., 2012). However, few efforts have been committed to its application in electrochemical sensors, which is probably ascribed to its relatively poor electron mobility (0.3 $cm^2 V^{-1} s^{-1}$ for rutile TiO_2) and low specific surface area (Wang et al., 2013; Xu et al., 2012). To enhance the charge separation and conductivity of TiO_2 nanomaterials, chemical doping of metal ions has been applied as a highly promising approach during the past few years (D'Souza et al., 2016; Sasani et al., 2016; Zhou et al., 2016). For instance, Wang et al. prepared tungsten-doped TiO_2 core-shell nanowires with a simultaneous hydrothermal etching and doping method (Wang et al., 2013). Tungsten species were incorporated into the

* Corresponding authors.
E-mail addresses: 13781157777@163.com (X. Liu), hxju@nju.edu.cn (H. Ju).

http://dx.doi.org/10.1016/j.bios.2017.02.019
Received 30 November 2016; Received in revised form 8 February 2017; Accepted 13 February 2017
Available online 14 February 2017

amorphous TiO_2 shell during the simultaneous etching/regrowth step for the optimization of PEC performance. In particular, electrochemical impedance spectroscopic results demonstrated the enhancement of the charge transfer of TiNWs by Tungsten doping.

The successful application of graphene in various fields has stimulated enormous interests in the preparation of analogous nanomaterials to obtain certain unusual properties. Molybdenum disulfide (MoS_2) is one of typical graphene analogs due to its special geometric structure, which is composed of Mo metal layers sandwiched between two sulfur layers via weak van der Waals interaction (Song et al., 2014; Yang et al., 2016). Accordingly, MoS_2 crystals have shown many outstanding properties comparable to those of graphene such as excellent electronic performance, unusual optical properties, robust mechanical properties and easy surface modification (Bertolazzi et al., 2011; Loo et al., 2014; Radisavljevic et al., 2011; Yin et al., 2012). Although MoS_2 has been introduced in various electrochemical fields including transistors, fuel cell and energy storage (Xu et al., 2009; Yu et al., 2015), and a laccase biosensor has been prepared with a nanocomposite of molybdenum disulfide (MoS_2) and graphene quantum dots (GQDs) for enzyme immobilization (Vasilescu et al., 2016), its application in electrochemical sensing is very limited.

In this work, the properties of TiNW arrays were significantly improved by a simultaneous"etching, doping and deposition"method, which led to a new type of immunosensor platform by coating chitosan (a biocompatible polysaccharide with amino groups), and then immobilizing capture antibody on the electrode surface using bis(sulfosuccinimidyl) suberate sodium salt (BS^3) as amino cross-linking reagent. The tracing labels were prepared by co-immobilizing signal antibody and HRP on cylinder-shaped TiO_2 nanorods with high surface area and good biocompatibility. The proposed immunosensor showed excellent amperometric performance for CEA detection, indicating promising application of the immunosensing platform in sensitive determination of tumor biomarkers.

2. Experimental

2.1. Material and reagents

Mouse monoclonal capture anti-CEA antibody (Ab1, clone no. 21D6), signal anti-CEA antibody (Ab2, clone no. 24D2) and CEA (98%, Product no. A0102) were purchased from Shuangliu Zhenglong Biochem. Lab (Chengdu, China). They were immediately diluted to the required concentrations with 0.02 M pH 7.4 phosphate buffer solution (PBS) prior to use. Commercial fluorine-doped tin oxide (FTO) glasses (1.1 mm thickness, 10 Ω/sq sheet resistance) were obtained from Wuhan Lattice Solar Energy Techonology, Ltd., China. Concentrated hydrochloric acid (37 wt%), tetrabutyl titanate, hydroxylamine hydrochloride ($NH_2OH{\cdot}HCl$), and titanium tetrachloride were ordered from Tianjin Chemical Reagent Co., Ltd., China. Sodium sulfide nonahydrate ($Na_2S{\cdot}9H_2O$), and sodium molybdate dihydrate ($Na_2MoO_4{\cdot}2H_2O$) were purchased from Aladdin reagent co., Ltd., China. Polyethylene glycol, chloroform, absolute ethanol and 30% H_2O_2 (v/v) were ordered from Sinopharm Chemical Reagent Co. Ltd., China. Hydroquinone and ammonia (28%) were obtained from J & K Scientific Ltd. (Beijing, China). 3-aminopropyltriethoxysilane (APTES), BS^3, HRP, bovine serum albumin (BSA), and chitosan (CS, 85% deacetylation) were all ordered from Sigma-Aldrich Chemical Co. (St. Louis, MO, USA). Ultrapure water obtained from a Millipore water purification system (≥18 MΩ, Milli-Q, Millipore) was used in all assays. All other reagents were of analytical grade and used as received. The PBS was prepared by mixing the stock solutions of 0.05 M KH_2PO_4 and 0.05 M K_2HPO_4 containing 0.1 M KCl as the supporting electrolyte. The washing buffer (PBST) consisted of PBS (0.05 M, pH 7.0) and 0.05% (w/v) Tween 20, and the blocking solution was PBS (0.05 M, pH 7.0) containing 5% (w/v) BSA.

2.2. Apparatus

All electrochemical measurements were performed using a CHI630C electrochemical workstation (Shanghai CH Instruments, China) with the modified FTO glasses as working electrodes. Electrochemical impedance spectroscopic measurements were carried out at an IM6ex electrochemical station (ZAHNER, Germany). The morphologies and chemical composition of the materials were examined by scanning electron microscopy (SEM, JSM-7610F, Japan), transmission electron microscope (TEM, Tecnai G2 20, USA), X-ray diffraction (XRD, Bruker D8 Advance, Germany) with Cu Kα radiation, and Fourier transform infrared spectra (FT-IR, Nicolet 170, USA). X-ray photoelectron spectra (XPS) were collected on an X-ray photoelectron spectrometer (ESCALAB 250Xi, USA) with a monochromated Al Kα source (hν=1486.6 eV, 150 W Power and 500 μm beam spot). The spectra were calibrated on the C1s peak (284.8 eV) and analyzed by XPSPEAK41 software.

2.3. Preparation of TiO_2 nanowire arrays

The rutile TiO_2 nanowire arrays were synthesized on FTO glass substrates by a previously reported hydrothermal method with minor modification (Liu and Aydil, 2009). Before the synthesis, a few slices of FTO substrate were cleaned ultrasonically with acetone, ethanol and deionized water alternately, and dried under a N_2 stream. After that, 13 mL of concentrated HCl (37 wt%) was diluted by 15 mL of deionized water, and stirred for 5 min under room temperature. Then 300 μL of tetrabutyl titanate was added in the diluted HCl, followed by 15 min of constant stirring. Subsequently, the mixture solution and the cleaned FTO glass substrates were transferred into a 50 mL sealed Teflon-lined stainless steel autoclave, which was kept in an oven at 150 ℃ for 12 h. The FTO substrates covered with a thin layer of white uniform film were taken out from the autoclave, rinsed with deionized water and dried in compressed N_2 stream.

2.4. Simultaneous "etching, doping and deposition" modification of TiNW arrays

The procedure of triplex modification of TiNW arrays is displayed in Scheme 1A. A mixture containing 30 mL of deionized water, 0.725 g of hydroxylamine hydrochloride ($NH_2OH{\cdot}HCl$), 1.70 g of sodium sulfide nonahydrate ($Na_2S{\cdot}9H_2O$), 0.48 g of sodium molybdate dihydrate ($Na_2MoO_4{\cdot}2H_2O$), and 50 μL polyethylene glycol was placed in a 50 mL sealed Teflon-lined stainless steel autoclave together with the TiNW arrays modified FTO substrates. The autoclave was kept at 250 ℃ for 24 h, and the FTO substrates were then taken out and thoroughly washed with deionized water. Obviously, a layer of black sediment was coated on TiNW arrays. The reaction formulas for MoS_2 formation, including reduction, sulfuration and precipitation, were shown in Supporting Information.

2.5. Preparation of TiO_2 nanorods and tracing label

The cylinder-shaped TiO_2 nanorods were synthesized by a facile hydrothermal method reported previously (Yang et al., 2015). The preparation procedures of both TiO_2 nanorods and their amination were described in the Supporting Information. The preparation of the tracing label was shown in Scheme 1B. Specifically, 3 mg of amino-functionalized TiO_2 nanorods was dispersed in 1 mL BS^3 (2 mg mL^{-1}) solution. 300 μL of HRP (2 mg mL^{-1}) was then mixed with the dispersion, and the mixture was incubated for 0.5 h. Afterward, 20 μL Ab2 (0.5 mg mL^{-1}) was added into the mixture, followed by incubation at 4 ℃ for 8 h under gentle stirring. After centrifugation, the obtained bioconjugate was washed with PBS and blocked with 2% BSA for 30 min at room temperature. Finally, the bioconjugate was washed with PBS again and resuspended in 1.0 mL PBS containing 0.1% BSA.

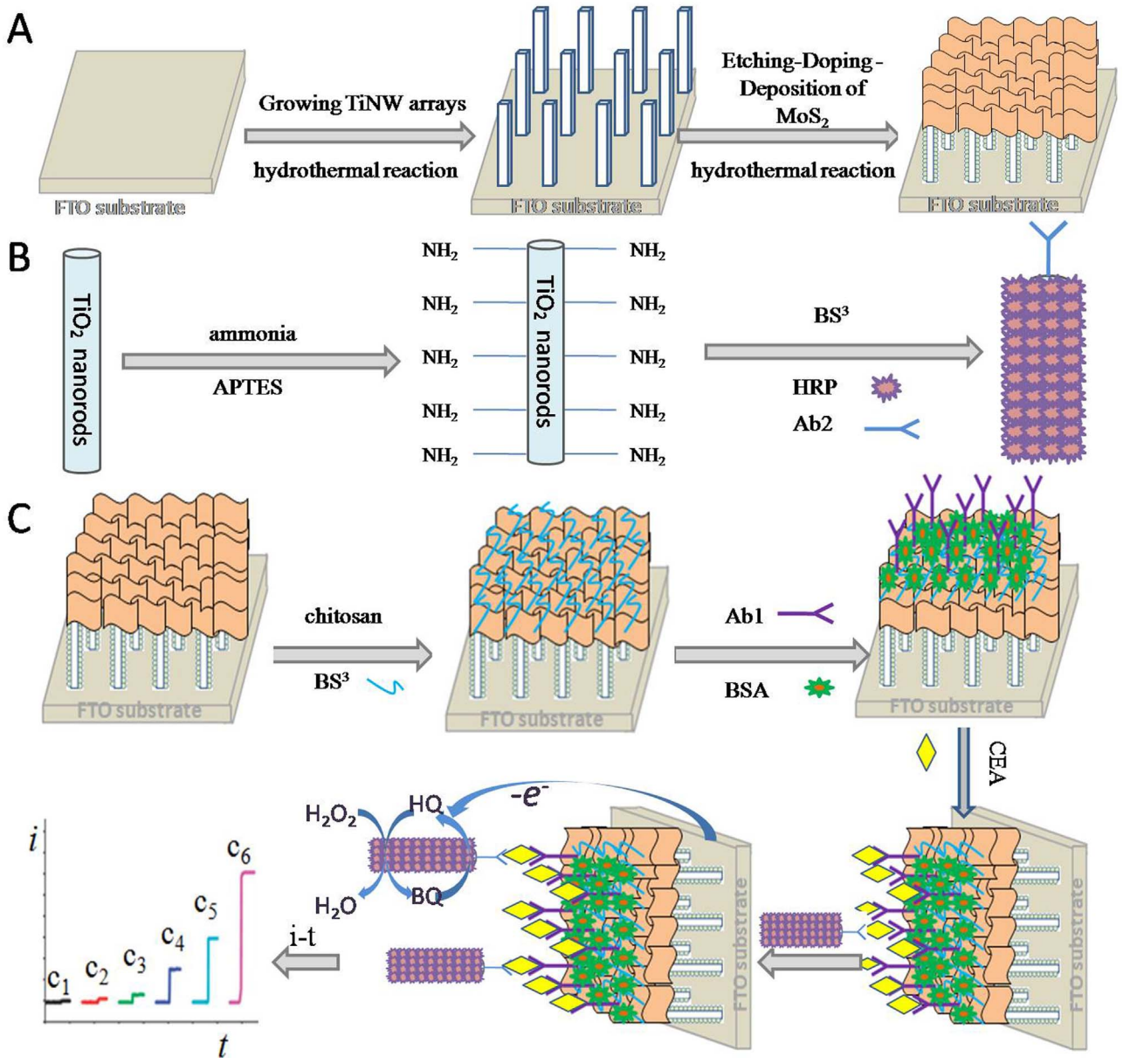

Scheme 1. Schematic illustration for (A) triplex modification of TiNW arrays, (B) preparation of tracing label, and (C) assembly and detection procedures of immunosensor for CEA.

2.6. Assembly of CEA immunosensor

A droplet of 30 μL 0.3 wt% CS solution (in 1% acetic acid) was cast on the triply modified TiNW arrays and dried under ambient environment. Then 30 μL BS^3 solution (2 mg mL^{-1}) was incubated on the array electrode surface for 1 h at room temperature. Subsequently, 30 μL Ab1 (0.38 mg mL^{-1}) was immediately dropped on the modified electrode, which was left at room temperature for another 1 h and then stored at 4 °C overnight in refrigerator. The immunosensor was washed with PBST and PBS successively to remove the physically absorbed Ab1. After that, 20 μL blocking solution was incubated on the immunosensor surface for 60 min at room temperature to block possible remaining active sites against nonspecific adsorption. The as-prepared immunosensor was washed with PBST and PBS respectively, and stored at 4 °C for later use.

2.7. Immunoassay procedure

As shown in Scheme 1C, the immunosensor was incubated with certain concentration of CEA (30 μL) at room temperature for 50 min, and then washed carefully with PBST and PBS respectively. It was then incubated with 30 μL of labeled Ab2 for 1 h at room temperature and rinsed with PBST and PBS successively. Finally, the immunosensor, Ag|AgCl reference electrode and Pt counter electrode were placed in an electrochemical cell containing 5 mL PBS, 1 mM H_2O_2 and 2 mM hydroquinone. The mixed solution was deoxygenized with high purity nitrogen for 20 min to perform the electrochemical measurement in nitrogen atmosphere at a constant potential of −0.2 V.

3. Results and discussion

3.1. Microscopic characterization

The SEM and TEM photos were obtained to characterize the morphologies of TiNW arrays and TiO_2 nanorods. As shown in Fig. 1, both the plane-view (A) and the side-view (B) images of pristine TiNW arrays demonstrated that the white film formed on FTO consisted of dense and vertically aligned nanowire arrays, which exhibited nearly rectangular cross sections. The average diameter and length of these nanowires were estimated to be ~150–180 nm and

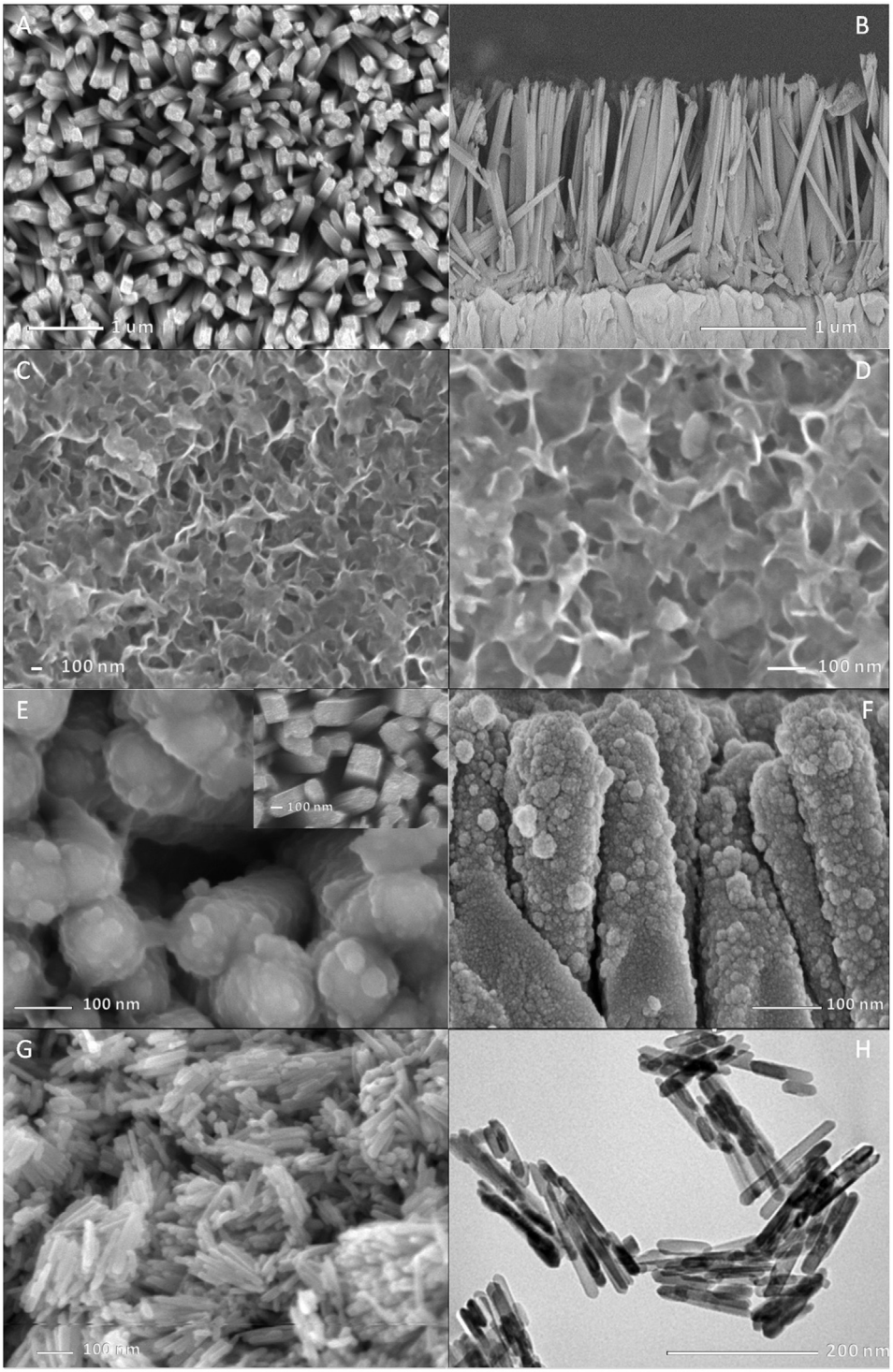

Fig. 1. (A) Plane-view and (B) side-view SEM images of pristine TiNW arrays. (C, D) SEM images of MoS_2|etched-doped TiNW arrays at two scales. (E) Plane-view and (F) side-view SEM images of etched-doped TiNW arrays. (G) SEM and (H) TEM images of cylinder-shaped TiO_2 nanorods.

~1.5–2 μm, respectively. After the simultaneous "etching, doping and deposition" modification, the surface of TiNW arrays was covered by a layer of black sediment, as confirmed by Fig. 1C and D. The black sediment exhibited honeycomb layered structure with a large specific surface area of ~156 $m^2 g^{-1}$ (BET method), which was much larger than that of TiNW arrays (~85 $m^2 g^{-1}$). After the triply modified TiNW arrays were immersed in an aqua regia solution for 24 h, the plane-view and the side-view SEM images (Fig. 1E and F) indicated that the black sediment was completely removed, and the shape of TiNWs was changed from rectangle to cylinder with an average diameter of ~100–120 nm. Furthermore, TiNW surface was fully covered by granules, attributing to the etching out and regrowing of TiNW arrays (Wang et al., 2013). The SEM and TEM images of TiO_2 nanorods (Fig. 1G and H) showed the uniform cylinder-like morphology with average diameter of ~20 nm and length of ~180 nm.

3.2. XPS characterization of pristine TiNW and modified TiNW arrays

To confirm the simultaneous Mo doping and MoS_2 deposition on

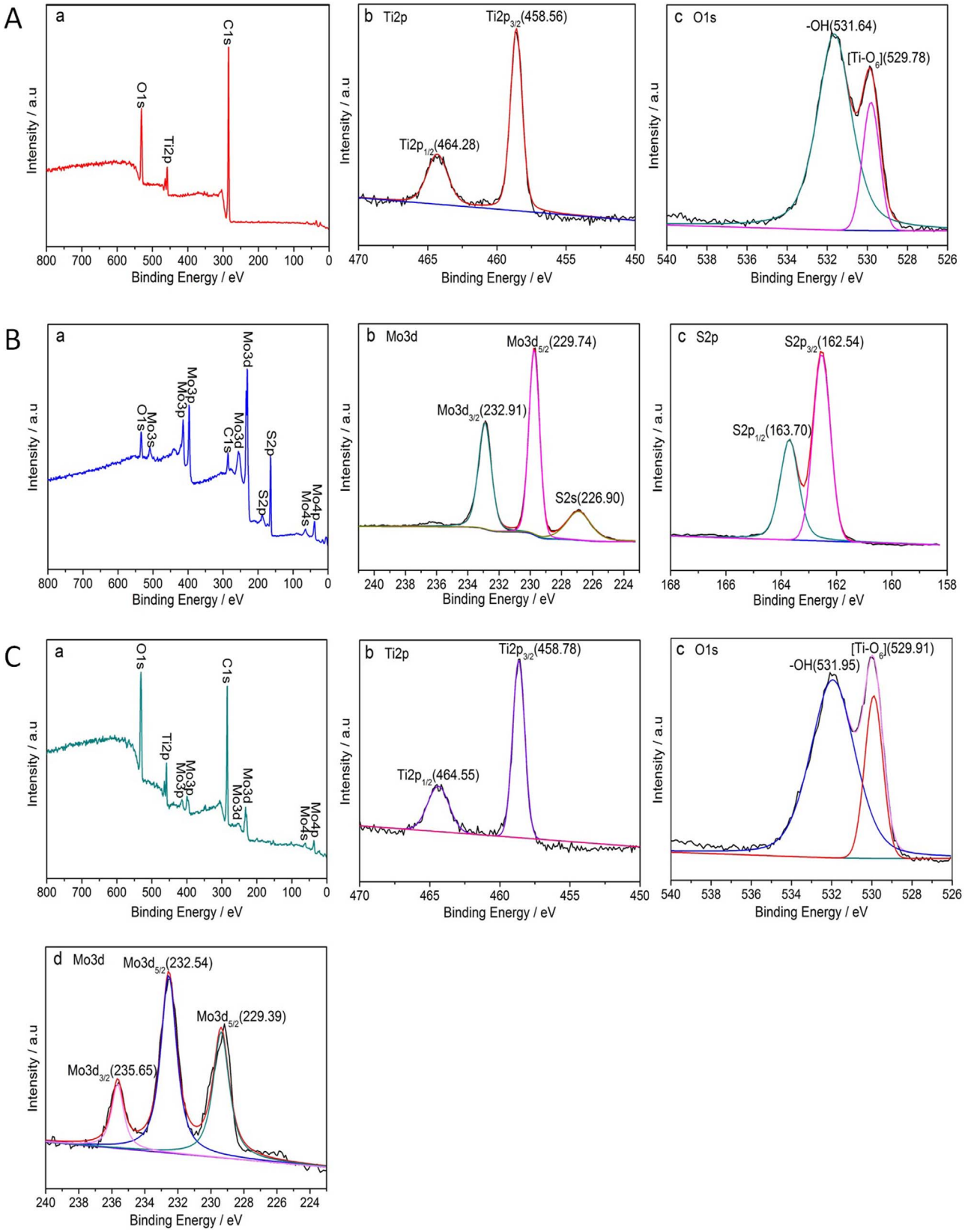

Fig. 2. XPS spectra of (A) pristine TiNW arrays: (a) XPS survey spectrum, and high-resolution XPS spectra of (b) Ti2p, and (c) O1s; (B) triply modified TiNW arrays: (a) XPS survey spectrum, high-resolution XPS spectra of (b) Mo3d, (c) S2p; and (C) etched-doped TiNW arrays: (a) XPS survey spectrum, high-resolution XPS spectra of (b) Ti2p, (c) O1s, and (d) Mo3d.

TiNWs, the elemental composition of the nanomaterials was investigated by XPS. The survey scan of pristine TiNWs (Fig. 2A(a)) demonstrated that the samples were mainly composed of Ti and O elements. As depicted in Fig. 2A(b), pristine TiNW displayed two typical peaks of Ti2p centered at 458.56 and 464.28 eV, which were assigned to $Ti2p_{3/2}$ and $Ti2p_{1/2}$ (Aragaw et al., 2015; Chen et al., 2011). The O1s peaks at

529.78 and 531.64 eV (Fig. 2A(c)) corresponded to the lattice oxygen [Ti-O_6] in the TiNW and hydroxyl oxygen atoms from TiNW surface respectively (Aragaw et al., 2015; Chen et al., 2011). These results confirmed the successful formation of TiNW arrays on FTO.

After the simultaneous "etching, doping and deposition", the high-resolution XPS spectra of the samples indicated that the predominant elements on the modified FTO were Mo and S (Fig. 2B(a)), which exhibited an atomic ratio of ~1:2. The high resolution spectrum of Mo (Fig. 2B(b)) displayed two peaks at 229.74 and 232.91 eV, attributing to $Mo3d_{5/2}$ and $Mo3d_{3/2}$ of Mo^{4+} species in MoS_2 (Weng et al., 2015; Xu et al., 2014; Yin et al., 2016). The third peak located at 226.9 eV was probably ascribed to S2s (Weng et al., 2015; Xu et al., 2014). The XPS spectrum of S element was fitted into $S2p_{1/2}$ and $S2p_{3/2}$ peaks (Fig. 2B(c)), which appeared at 163.7 and 162.54 eV, respectively (Weng et al., 2015; Yin et al., 2016). Thus, the successful deposition of MoS_2 on top of TiNW arrays after the triplex modification was demonstrated.

To confirm the doping of Mo in TiNWs during the "etching, doping and deposition" procedure, MoS_2 flakes coated on TiNW arrays were removed by the aqua regia solution. After thoroughly washed with distilled water and dried under N_2 stream, the bare TiNW arrays were characterized with XPS, as displayed in Fig. 2C. The survey scan indicated the presence of Ti, O and Mo elements (Fig. 2C(a)). After doped with Mo element, the binding energy of $Ti2p_{3/2}$ and $Ti2p_{1/2}$ peaks shifted to 458.78 and 464.55 eV (Fig. 2C(b)), probably attributing to the substitution of Ti atoms by less electronegative Mo atoms. Similar to pristine TiNWs, Mo doped TiNW arrays exhibited two O1s peaks at 529.91 and 531.95 eV (Fig. 2C(c)), ascribing to the lattice oxygen [Ti-O_6] in TiNW and the O from Ti-OH groups on TiNW surface. The high resolution spectrum of Mo (Fig. 2C(d)) displayed three peaks at 235.65 eV, 232.54 eV and 229.37 eV, corresponding to $Mo3d_{3/2}$, $Mo3d_{5/2}$ and $Mo3d_{5/2}$ respectively (Gao et al., 2011). These results demonstrated that the Mo element was successfully doped in TiNWs during the"etching, doping and deposition"process.

3.3. XRD characterization of FTO substrate and the materials

XRD spectroscopy was used to study the crystal structure of TiNW arrays and verify the deposition of MoS_2 on TiNW arrays. Bare FTO substrate (Fig. 3A(a)) displayed several diffraction peaks at ~13.12° , 26.35° , 37.72° , 51.49° , 61.59° , 65.62°, which were derived from SnO_2 phase in FTO and labeled by asterisks for comparison purpose. The pristine TiNW arrays grown on FTO substrate showed two typical diffraction peaks at 36.1°and 62.7° (Fig. 3A(b)), in accord with the (101) and (002) crystal face reflections of tetragonal rutile TiO_2 (Chang et al., 2012; Li et al., 2013; Yun et al., 2016). After the triplex modification, the XRD pattern of MoS_2 on TiNW surface (Fig. 3A(c)) exhibited three obvious peaks at 14.5°, 33.8° and 59.5°, corresponding to the (002), (100) and (110) crystal faces of MoS_2 (Altavilla et al., 2011; Qi et al., 2016; Wei et al., 2016). Finally, MoS_2 flakes on TiNW arrays were removed in aqua regia solution to investigate the crystal form of Mo doped TiNW arrays. As shown in Fig. 3A(d), Mo doped TiNW arrays presented very similar XRD pattern as that of the pristine TiNW arrays (Fig. 3A(b)), indicating negligible change of TiNW crystal form after Mo doping and the strong acid treatment. The XRD pattern of cylinder-shaped TiO_2 nanorods also indicated the rutile crystal form of the prepared samples (Fig. S1 in the Supporting Information).

3.4. EIS investigation of immunosensor assembly process

As a reliable technique for investigating the interfacial properties of modified electrodes, electrochemical impedance spectroscopy (EIS) was employed herein to monitor the stepwise assembly process of the CEA immunosensor. The immunosensor fabrication was illustrated in Scheme 1C and detailed in Experimental section. Impedance experiments were performed in 0.1 M KCl solution containing 5 mM $K_3[Fe(CN)_6]|K_4[Fe(CN)_6]$ with the frequency scanned from 100 kHz to 100 mHz at a DC potential of 0.230 V superimposed by a 5 mV alternating voltage. The Nyquist plots showed a semicircle at high frequency region and a linear portion at low frequency region (Fig. 3B). Among all the electrodes, the bare FTO (curve a) displayed the smallest semicircle, indicating the smallest electron transfer resistance (R_{et}). On the contrary, the pristine TiNW array coated FTO (curve f) exhibited the maximum R_{et}, which implied the lowest electrical conductivity of TiO_2. Most interestingly, after the simultaneous "etching, doping and deposition" modification of TiNW arrays, the R_{et} of the modified TiNW|FTO (curve b) obviously decreased, demonstrating that the triply modification of TiNW arrays significantly enhanced their conductivity. With the sequential immobilizing of Ab1 (curve c), BSA (curve d) and labeled Ab2 (curve e) on MoS_2|etched-doped TiNW|FTO, the R_{et} gradually increased. The low conductivity and steric hindrance effect of the immobilized proteins obstructed the mass transport and electron transfer of the electrochemical probe to the electrode surface. All the above results indicated the successful fabrication of CEA immunosensor and the significant conductivity improvement of TiNW arrays after the triplex modification.

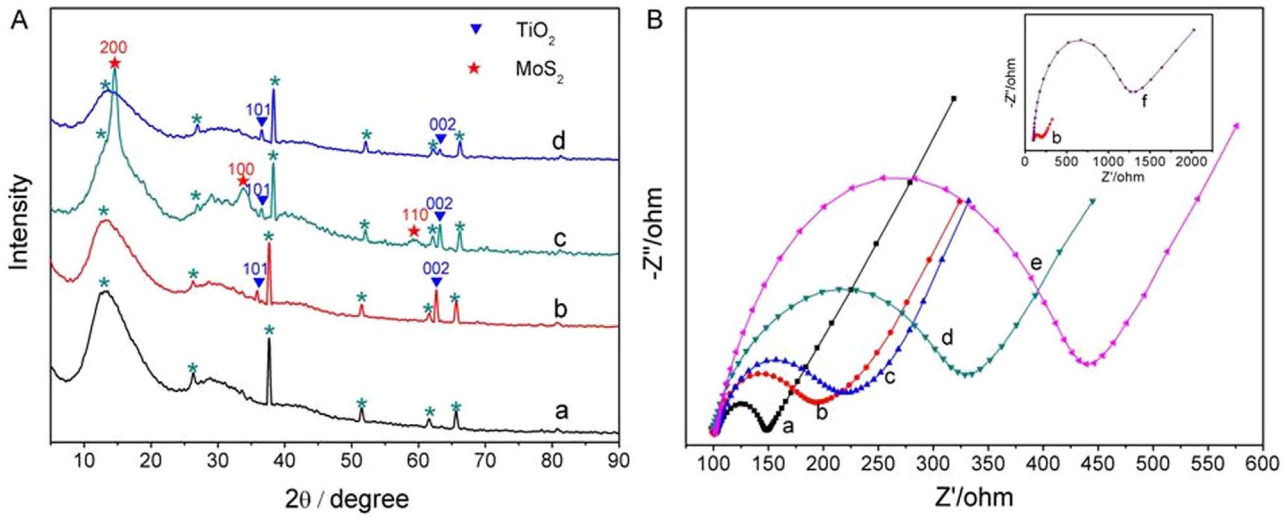

Fig. 3. (A) XRD pattern of (a) bare FTO substrate, (b) pristine TiNW arrays, (c) triply modified TiNW arrays, and (d) etched-doped TiNW arrays. (B) Nyquist plots of (a) bare FTO, (b) MoS_2|etched-doped TiNW|FTO, (c) Ab1|MoS_2|etched-doped TiNW|FTO, (d) immunosensor, (e) labeled Ab2|CEA|immunosensor, and (f) pristine TiNW|FTO.

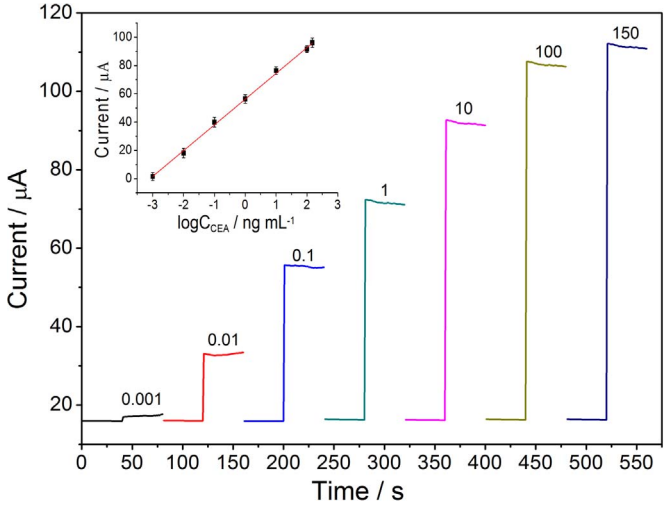

Fig. 4. Amperometric response-time plot for the proposed immunosensors incubated with increasing concentration of CEA from 0.001 to 150 ng mL^{-1} at a applied potential of −0.2 V. Inset: Plot of current signal versus logarithm of CEA concentration. The errors are obtained from six parallel tests.

3.5. Optimization of operation conditions for immunosensing

Several important experimental parameters including pH value of the test solution, incubation time of CEA, concentration of Ab1 and the ratio of HRP to Ab2 were optimized before the final performance evaluation (Fig. S2, the Supporting Information). Finally, 0.05 M PBS (pH 7.0) containing 0.10 M KCl, an incubation time of 50 min, 0.38 mg mL^{-1} Ab1 and a volume ratio of 15 of HRP to Ab2 were selected in the subsequent measurements.

3.6. Quantitative determination of CEA

Under the optimum conditions, the current response of the immunosensor rapidly reached a steady state upon the addition of H_2O_2 (Fig. 4), and increased linearly with the increasing logarithm value of CEA concentration from 0.001 to 150 ng mL^{-1} with a detection limit of 0.5 pg mL^{-1} (S/N=3) (inset of Fig. 4). Six parallel tests were conducted at each concentration point and the current response for total seven increasing concentration points was collected to obtain the calibration plot. The analytical performance of the CEA immunosensor was superior to many previously reported methods, as listed in Table 1. The triplex modification of TiNW not only improved the electronic conductivity of the immunosensing platform, but also increased the specific surface area of the platform to immobilize substantial quantity of biomolecules. Therefore, the triply modified TiNW arrays were expected to be a promising immunosensing platform for the future application. It was also observed that the immunosensor without using TiO_2 nanorod tracing label exhibited a dynamic range of 0.5–80 ng mL^{-1} and a detection limit of 26 pg mL^{-1}. These results were much poorer than those of the immunosensor using TiO_2 nanorod tracing labels, demonstrating the strong signal enhancement effect of the tracing label.

3.7. Reproducibility, selectivity, stability and practical test of the immunosensor

The reproducibility of the proposed CEA immunosensor was evaluated by measuring the same sample with five sensors prepared independently in the identical experimental conditions. A relative standard deviation (RSD) of 5.7% was obtained, suggesting an acceptable precision of the immunosensor fabrication. The selectivity of the immunosensor was assessed by mixing one of the following possible interferences including α-Fetoprotein (AFP), prostate protein antigen (PSA), cinoma antigen 125 (CA125), immunoglobulin G (IgG) and BSA into the standard samples. The immunosensor was then incubated with a solution of 1.0 ng mL^{-1} CEA containing one of the above interferences (20 ng mL^{-1}), which showed less than 5.1% current signal variation (Fig. S3, the Supporting Information), demonstrating the good selectivity of the immunosensor. After these immunosensors were stored at 4 °C for 15 days, 91.4% of the initial current was retained, indicating the good stability of the immunosensor. After 0.1, 1 and 10 ng mL^{-1} CEA was spiked into serum samples respectively, the immunosensor showed a recovery of 95.6–106.3% (Table S1), implying the application possibility of the immunosensor in the clinical detection of CEA.

Table 1
Comparison of the proposed immunosensor with other CEA immunosensors.

Immunosensors	Linear range (ng mL^{-1})	Limit of detection (pg mL^{-1})	References
GCE/chitosan-gold/GA/Ab1/CEA/Cu-CP[a]-Ab2	0.1–100	20	(Rong et al., 2016)
GCE/GO-AuNPs/Ab1/CEA/Fe_3O_4@SiO_2–Fc–Ab2 /HRP	0.001–80	0.2	(Feng et al., 2016)
FTO/TiO_2/CdS:Mn[b]/CS/GA/Ab1/ CEA/AgNCs-GR[c]-Ab2	0.001–100	1	(Song et al., 2016)
GCE/PTh-Au[d]/Ab1/BSA/CEA	0.005–40	2.2	(Cai et al., 2016)
GCE/PAMAM-Au-PBA[e]-ARS[f]/ Ab1/CEA/Am[g]-Au-Ab2	0.01–50	3	(Zhang and Ding, 2016)
GCE/AuNPs/Ab1/CEA/HRP-GO-Ab2	0.001–80	0.64	(Hou et al., 2013)
GCE/HDGM[h]/Ab1/CEA/HRP– GNPG[i]–Ab2	0.005–80	5	(Chen et al., 2013)
GCE/HSO_3-GS[j]/thionine/CS-PdCu/Ab1/ BSA/ CEA	0.01–12	4.86	(Cai et al., 2012)
GCE/thionine/CNS-GNS[k]/Ab1/ CEA/HPtNS[l]-HRP-Ab2	0.001–100	1	(Zhou et al., 2012)
Label Ab2/CEA/Ab1/etched-doped TiNW arrays/FTO	0.001–150	0.5	This work

[a] Copper ions doped chitosan–poly(acrylic acid) nanospheres.
[b] Mn^{2+} doped CdS QDs modified TiO_2.
[c] Silver nanocluster/graphene nanocomposite.
[d] Polythionine-Au composites.
[e] 4-mercaptophenylboronic acid.
[f] Alizarin Red S.
[g] Amylase.
[h] Hierarchical dendritic gold microstructures.
[i] Graphene oxide-poly(*o*-phenylenediamine)- nanogold hybrid nanosheets.
[j] Sulfonated grapheme.
[k] Nano carbon-graphene hybrid nanomaterials.
[l] Hollow platinum nanospheres.

4. Conclusion

In this work, TiNW arrays have been etched and doped with Mo, and deposited by MoS_2 flakes using a one-pot hydrothermal method. SEM, TEM, XPS and XRD characterization has evidenced the successful Mo-doping and MoS_2 deposition during the hydrothermal reaction. EIS measurements confirmed the stepwise assembly process of the immunosensor. The immunosensor has been used for ultrasensitive detection of a model analyte, CEA, which shows a performance superior to many reported CEA immunosensors. Specifically, the synergistic effect of etching, Mo-doping and deposition of two-dimensional thin-layer MoS_2 flakes have significantly enhanced the charge transfer and electronic conductivity of TiNW arrays coated on FTO. The triply modified TiNW arrays also provided a biocompatible microenviroment for the biomolecules and increased specific surface area of the electrode, which retained the bioactivity and promoted the immobilization of biomolecules. All of above advantages have contributed to the improvement of the immunosensor performance.

Acknowledgments

This work was financially supported by National Natural Science Foundation of China (No. U1504215), the Scientific Research Foundation for the Returned Overseas Chinese Scholars, State Education Ministry (Batch 46th), and the grant from College Science and technology Innovation Team Program of Henan Province (No. 141RTSTHN030) and the Open Research Funding of State Key Laboratory of Analytical Chemistry for Life Science, Nanjing University, China (No. SKLACLS1409).

Appendix A. Supplementary material

Supplementary data associated with this article can be found in the online version at http://dx.doi.org/10.1016/j.bios.2017.02.019.

References

Altavilla, C., Sarno, M., Ciambelli, P., 2011. Chem. Mater. 23, 3879–3885.
Aragaw, B.A., Pan, C.-J., Su, W.-N., Chen, H.-M., Rick, J., Hwang, B.-J., 2015. Appl. Catal., B 163, 478–486.
Bertolazzi, S., Brivio, J., Kis, A., 2011. ACS Nano 5, 9703–9709.
Cai, X., Weng, S., Guo, R., Lin, L., Chen, W., Zheng, Z., Huang, Z., Lin, X., 2016. Biosens. Bioelectron. 81, 173–180.
Cai, Y., Li, H., Li, Y., Zhao, Y., Ma, H., Zhu, B., Xu, C., Wei, Q., Wu, D., Du, B., 2012. Biosens. Bioelectron. 36, 6–11.
Chang, M., Wu, L., Li, X., Xu, W., 2012. J. Mater. Sci. Technol. 28, 594–598.
Chen, H., Gao, Z., Cui, Y., Chen, G., Tang, D., 2013. Biosens. Bioelectron. 44, 108–114.
Chen, X., Liu, L., Yu, P.Y., Mao, S.S., 2011. Science 331, 746–750.
D'Souza, L.P., Shwetharani, R., Amoli, V., Fernando, C.A.N., Sinha, A.K., Balakrishna, R.G., 2016. Mater. Des. 104, 346–354.
Da, P., Li, W., Lin, X., Wang, Y., Tang, J., Zheng, G., 2014. Anal. Chem. 86, 6633–6639.
Darain, F., Park, S.-U., Shim, Y.-B., 2003. Biosens. Bioelectron. 18, 773–780.
Feng, T., Qiao, X., Wang, H., Sun, Z., Hong, C., 2016. Biosens. Bioelectron. 79, 48–54.
Freedland, S.J., 2011. Cancer 117, 1123–1135.
Gao, H., Jiao, L., Peng, W., Liu, G., Yang, J., Zhao, Q., Qi, Z., Si, Y., Wang, Y., Yuan, H., 2011. Electrochim. Acta 56, 9961–9967.
Gao, Z.-D., Guan, F.-F., Li, C.-Y., Liu, H.-F., Song, Y.-Y., 2013. Biosens. Bioelectron. 41, 771–775.
Hou, L., Cui, Y., Xu, M., Gao, Z., Huang, J., Tang, D., 2013. Biosens. Bioelectron. 47, 149–156.
Huo, X., Liu, P., Zhu, J., Liu, X., Ju, H., 2016. Biosens. Bioelectron. 85, 698–706.
Li, N.-L., Jia, L.-P., Ma, R.-N., Jia, W.-L., Lu, Y.-Y., Shi, S.-S., Wang, H.-S., 2017. Biosens. Bioelectron. 89, 453–460.
Li, Y., Yu, H., Zhang, C., Fu, L., Li, G., Shao, Z., Yi, B., 2013. Int. J. Hydrog. Energy 38, 13023–13030.
Liu, B., Aydil, E.S., 2009. J. Am. Chem. Soc. 131, 3985–3990.
Loo, A.H., Bonanni, A., Ambrosi, A., Pumera, M., 2014. Nanoscale 6, 11971–11975.
Marquette, C.A., Blum, L.J., 2006. Biosens. Bioelectron. 21, 1424–1433.
Qi, Y., Xu, Q., Wang, Y., Yan, B., Ren, Y., Chen, Z., 2016. ACS Nano 10, 2903–2909.
Radisavljevic, B., Radenovic, A., Brivio, J., Giacometti, V., Kis, A., 2011. Nat. Nanotechnol. 6, 147–150.
Ramanathan, M., Patil, M., Epur, R., Yun, Y., Shanov, V., Schulz, M., Heineman, W.R., Datta, M.K., Kumta, P.N., 2016. Biosens. Bioelectron. 77, 580–588.
Rong, Q., Feng, F., Ma, Z., 2016. Biosens. Bioelectron. 75, 148–154.
Sasani, A., Baktash, A., Mirabbaszadeh, K., Khoshnevisan, B., 2016. Appl. Surf. Sci. 384, 298–303.
Song, H., Ni, Y., Kokot, S., 2014. Biosens. Bioelectron. 56, 137–143.
Song, J., Wang, J., Wang, X., Zhao, W., Zhao, Y., Wu, S., Gao, Z., Yuan, J., Meng, C., 2016. Biosens. Bioelectron. 80, 614–620.
Tang, J., Su, B., Tang, D., Chen, G., 2010. Biosens. Bioelectron. 25, 2657–2662.
Vasilescu, I., Eremia, S.A.V., Kusko, M., Radoi, A., Vasile, E., Radu, G.-L., 2016. Biosens. Bioelectron. 75, 232–237.
Wang, G.-L., Xu, J.-J., Chen, H.-Y., Fu, S.-Z., 2009. Biosens. Bioelectron. 25, 791–796.
Wang, Y., Ma, H., Wang, X., Pang, X., Wu, D., Du, B., Wei, Q., 2015. Biosens. Bioelectron. 74, 59–65.
Wang, Y., Zhang, Y.-Y., Tang, J., Wu, H., Xu, M., Peng, Z., Gong, X.-G., Zheng, G., 2013. ACS Nano 7, 9375–9383.
Wei, W., Samad, L., Choi, J.W., Joo, Y., Way, A., Arnold, M.S., Jin, S., Gopalan, P., 2016. Chem. Mater. 28, 4017–4023.
Weng, B., Zhang, X., Zhang, N., Tang, Z.-R., Xu, Y.-J., 2015. Langmuir 31, 4314–4322.
Xu, M., Da, P., Wu, H., Zhao, D., Zheng, G., 2012. Nano Lett. 12, 1503–1508.
Xu, X., Hu, J., Yin, Z., Xu, C., 2014. ACS Appl. Mater. Interfaces 6, 5983–5987.
Xu, Z.-R., Luo, J.-L., Chuang, K.T., 2009. J. Power Sources 188, 458–462.
Yang, T., Chen, M., Kong, Q., Luo, X., Jiao, K., 2016. Biosens. Bioelectron. 89, 538–544.
Yang, Z., Jian, Z., Chen, X., Li, J., Qin, P., Zhao, J., Jiao, Xa, Hu, X., 2015. Biosens. Bioelectron. 63, 190–195.
Yin, X.-L., Li, L.-L., Jiang, W.-J., Zhang, Y., Zhang, X., Wan, L.-J., Hu, J.-S., 2016. ACS Appl. Mater. Interfaces 8, 15258–15266.
Yin, Z., Li, H., Li, H., Jiang, L., Shi, Y., Sun, Y., Lu, G., Zhang, Q., Chen, X., Zhang, H., 2012. ACS Nano 6, 74–80.
Yu, X.-Y., Hu, H., Wang, Y., Chen, H., Lou, X.W.D., 2015. Angew. Chem. Int Ed. Engl. 54, 7395–7398.
Yun, G., Song, G.Y., Ahn, B.-E., Lee, S.-K., Heo, J., Ahn, K.-S., Kang, S.H., 2016. Appl. Surf. Sci. 366, 561–566.
Zhang, B., Ding, C., 2016. Biosens. Bioelectron. 82, 112–118.
Zhang, H., Zhao, Q., Li, X.-F., Le, X.C., 2007. Analyst 132, 724–737.
Zhao, L., Wei, Q., Wu, H., Dou, J., Li, H., 2014. Biosens. Bioelectron. 59, 75–80.
Zhou, J., Zhuang, J., Miró, M., Gao, Z., Chen, G., Tang, D., 2012. Biosens. Bioelectron. 35, 394–400.
Zhou, L., Wei, L., Yang, Y., Xia, X., Wang, P., Yu, J., Luan, T., 2016. Chem. Phys. 475, 1–8.
Zhuo, Y., Chai, Y.-Q., Yuan, R., Mao, L., Yuan, Y.-L., Han, J., 2011. Biosens. Bioelectron. 26, 3838–3844.